Correlative Microscopy: a tool for understanding soil weathering in modern analogues of early terrestrial biospheres

Mitchell, R. L[1, 2, 3]*., Davies, P*[1]*., Kenrick, P*[2]*., Volkenandt, T*[4]*., Pleydell-Pearce, C*[1]*., Johnston, R*[1]*.*

[1] Advanced Imaging of Materials (AIM) Facility, College of Engineering, Bay Campus, Swansea University, Swansea, SA1 8EN, UK (where work was completed).

[2] Earth Sciences Department, The Natural History Museum, Cromwell Road, London, SW7 5BD, UK.

[3] Sheffield Tomography Centre (STC), The University of Sheffield, North Campus, Broad Lane, Sheffield, S3 7HQ, UK (current address).

[4] Carl Zeiss Microscopy GmbH, Carl-Zeiss-Straße 22, 73447 Oberkochen, Germany.

Corresponding authors: r.mitchell@sheffield.ac.uk, r.johnston@swansea.ac.uk

ORCiD: RLM 0000-0002-6328-3998; PK 0000-0002-3626-5460; RJ 0000-0003-1977-6418; PD 0000-0003-3857-7801.

Abstract

Correlative imaging provides a method of investigating complex systems by combining analytical (chemistry) and imaging (tomography) information across dimensions (2D-3D) and scales (centimetres-nanometres). We studied weathering processes in a modern cryptogamic ground cover (CGC) from Iceland, containing early colonizing, and evolutionary ancient, communities of mosses, lichens, fungi, and bacteria. Targeted multi-scale X-ray Microscopy (XRM) of a grain in-situ within a soil core revealed networks of surficial and internal features (tunnels) originating from organic-rich surface holes. Further targeted 2D grain characterisation by optical microscopy (OM), scanning electron

25   microscopy (SEM), and energy dispersive X-ray spectroscopy (SEM-EDS), following an intermediate

26   manual correlative preparation step, revealed Fe-rich nodules within the tunnels. Finally,

27   nanotomographic imaging by focussed ion beam microscopy (FIB-SEM) revealed coccoid and

28   filamentous-like structures within subsurface tunnels, as well as accumulations of Fe and S in grain

29   surface crusts, which may represent a biological rock varnish/glaze. We attribute these features to

30   biological processes. This work highlights the advantages and novelty of the correlative imaging

31   approach, across scales, dimensions, and modes, to investigate biological weathering processes.

32   Further, we demonstrate correlative microscopy as a means of identifying fingerprints of biological

33   communities, which could be used in the geologic rock record and on extra-terrestrial bodies.

34

Introduction

36   Colonization of the land by plants and other organisms during the early Palaeozoic (~500 Ma[1])

37   was fundamental to the evolution of terrestrial landscapes. The expansion of primordial vegetation had

38   an influential effect on the architecture and evolution of river and sedimentary systems[2,3], weathering

39   and soil development[4–6], and crucially the drawdown of atmospheric CO_2 through organic carbon burial

40   and weathering[7,8]. The first plant-dominated biospheres were akin to modern cryptogamic ground

41   covers (CGCs)[4,9,10], which are composed of a consortia of early divergent and evolutionary ancient non-

42   vascular bryophyte plants (mosses, liverworts, hornworts), lichens, fungi, algae, and bacteria. At the

43   modern day, CGCs are present in a variety of habitats ranging from deserts to polar tundra[11–13], and

44   often are the pioneering organisms of bare land surfaces before the vascular plants. Modern CGCs are

45   considered suitable analogues for early terrestrial biotas because of the similarity between the modern

46   and ancient plant components (cryptophytes) and the relationships that they developed with other

47   organisms[4,10,14]. Importantly, symbioses between plants and fungi (e.g. mycorrhizae) and between fungi

48   and algae or cyanobacteria (e.g. lichens) were also present during the early Palaeozoic, with the

49   exceptionally preserved 407 million year old Rhynie chert biota providing many examples[15–17]. It is

50   generally regarded that symbionts in the early Palaeozoic were responsible for a portion of the

51   biologically mediated weathering via targeted nutrient (elemental) acquisition from soil minerals[18,19],

52   followed by development of the first biologically-mediated 'proto-soils'[13] and eventual global influence

53   on biogeochemical cycles[19,20]. However, the mechanisms of weathering in both the modern and ancient

54   examples are poorly understood. Investigating the intricate nano-to-micro scale interactions in modern

55   analogous CGCs can shed light on how ancestors of these primitive organisms contributed to soil-

56   forming processes, biologically mediated weathering, and potential nutrient-acquisition from their

57   substrates.

58   Previous research on modern CGCs developing on primordial land surfaces from Iceland (i.e.

59   lava flows and volcanic sedimentary terrains that are relatively new and unweathered land surfaces

60   devoid of 'higher' vascular plants) were mostly limited to 2D investigations, mainly of grain surface

61   processes[21]. These revealed biologically-mediated weathering features (BWFs) on volcanic glass and

62   scoria within soils that were attributed to the actions of different organisms (e.g. bacteria, fungi) and

63   processes (e.g. symbiosis, root-mediated dissolution)[21]. Prominent among these were 'tunnels', which

64   are thought to be created by 'boring' fungal hyphae[21–32]. These tunnels differ from holes that develop

65   naturally as gas-escape vesicles in volcanic ejecta because they generally form elongate tubes, are

66   associated with organic material, and are not present in every grain, and the tunnels are generally much

67   smaller than the vesicles. Here, we develop a novel correlative microscopy workflow across modes,

68   dimensions and scales to investigate the physical, chemical and morphological characteristics of these

69   tunnels. Our approach combines optical microscopy (OM), scanning electron microscopy (SEM)

70   imaging and chemical analysis (SEM-EDS), high resolution X-ray microscopy (tomography) (XRM)

71   and focussed ion beam microscopy (FIB-SEM), that are correlated using ZEISS ZEN Connect and Atlas

72   5 (3D) software. Correlative microscopy has the advantage that numerous data types can be acquired

73   and studied in-situ, in unison, and across dimensions, therefore providing a holistic approach, and

74   enabling a better understanding of how different parameters (e.g. morphology, chemistry, structure) are

75   linked. This approach is currently a developing application in human-made materials research[33–36] and

76   life/biological science[37–40], and despite a few geological[41–43] and more recently specific soil science

77   examples[44,45], the method has not been applied to soil weathering and biological interactions.

78   We adopt the following correlative strategy. First, we document the tunnel networks through

79   high resolution 3D XRM, which provides insights into their 3D morphology and how they might have

80   formed. Second, we show how 3D tomography can be correlated with high resolution imaging and

81   chemical data derived from SEM-EDS to provide information relating to the tunnel elemental variations

82   and micro-to-nano scale features. Finally, we utilise the correlative microscopy workflow to target

83   specific regions of interest for further analysis via FIB-SEM and generate nanotomographic volumes,

84   which not only increases resolution (small pixel/voxel sizes) but also provides complementary nested

85   3D information to XRM. Our aim is to use this correlative approach to characterize weathering,

86   potentially of a biological origin, in modern analogues of early land-plant communities. Our ultimate

87   goal is to develop the use of features on the micro-to-nanometre scale as fingerprints of biological

88   community presence and indicators of biologically mediated weathering in the geologic past. Further,

89   we propose that this approach could be used in the search for biological influences on extra-terrestrial

90   bodies.

91

92   **Results**
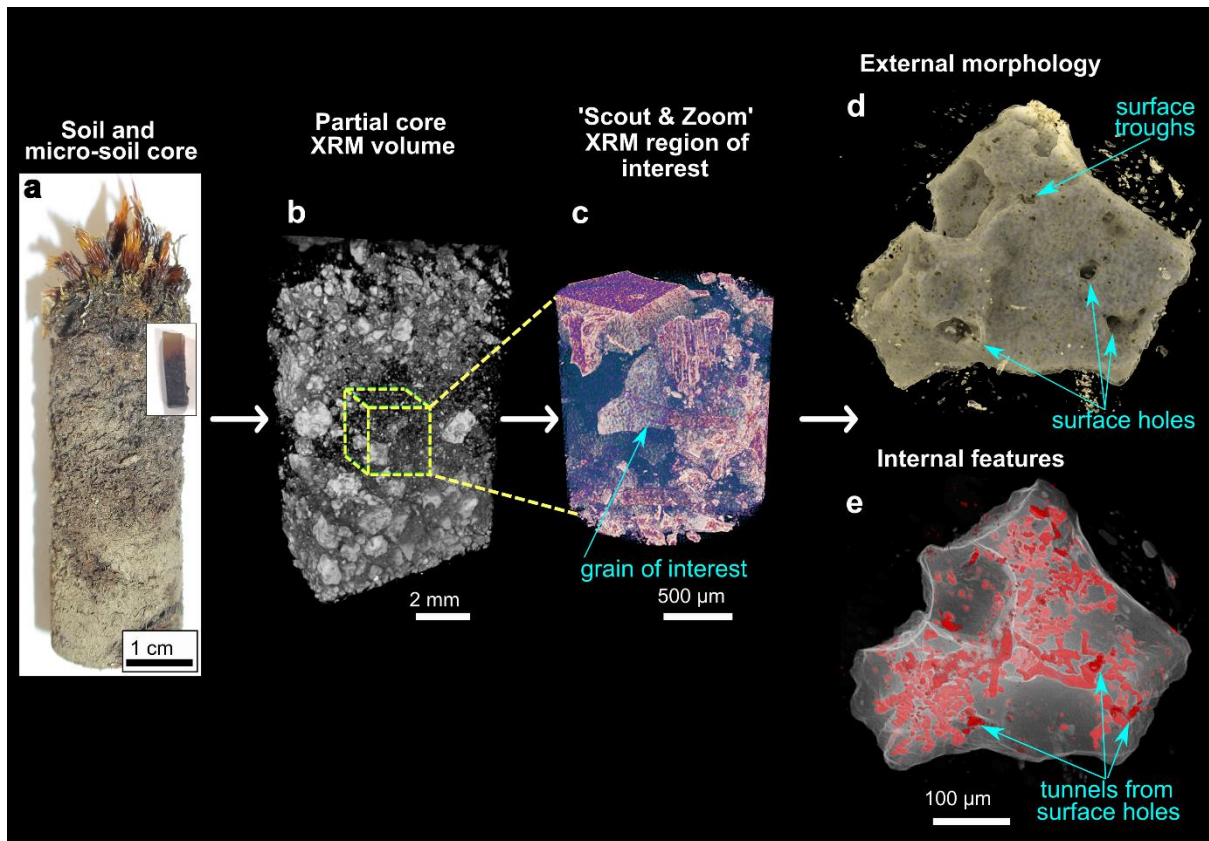
4

93

Figure 1. The correlative 3D imaging process: illustrates progressive higher resolution study from whole CGC soil core **(a),** to micro-core (inset), Scout and Zoom feature on ZEISS Xradia Versa 520 **(b, c),** and finally segmentation of grain tunnels **(d, e)** (also see Supplementary Videos S1-3).
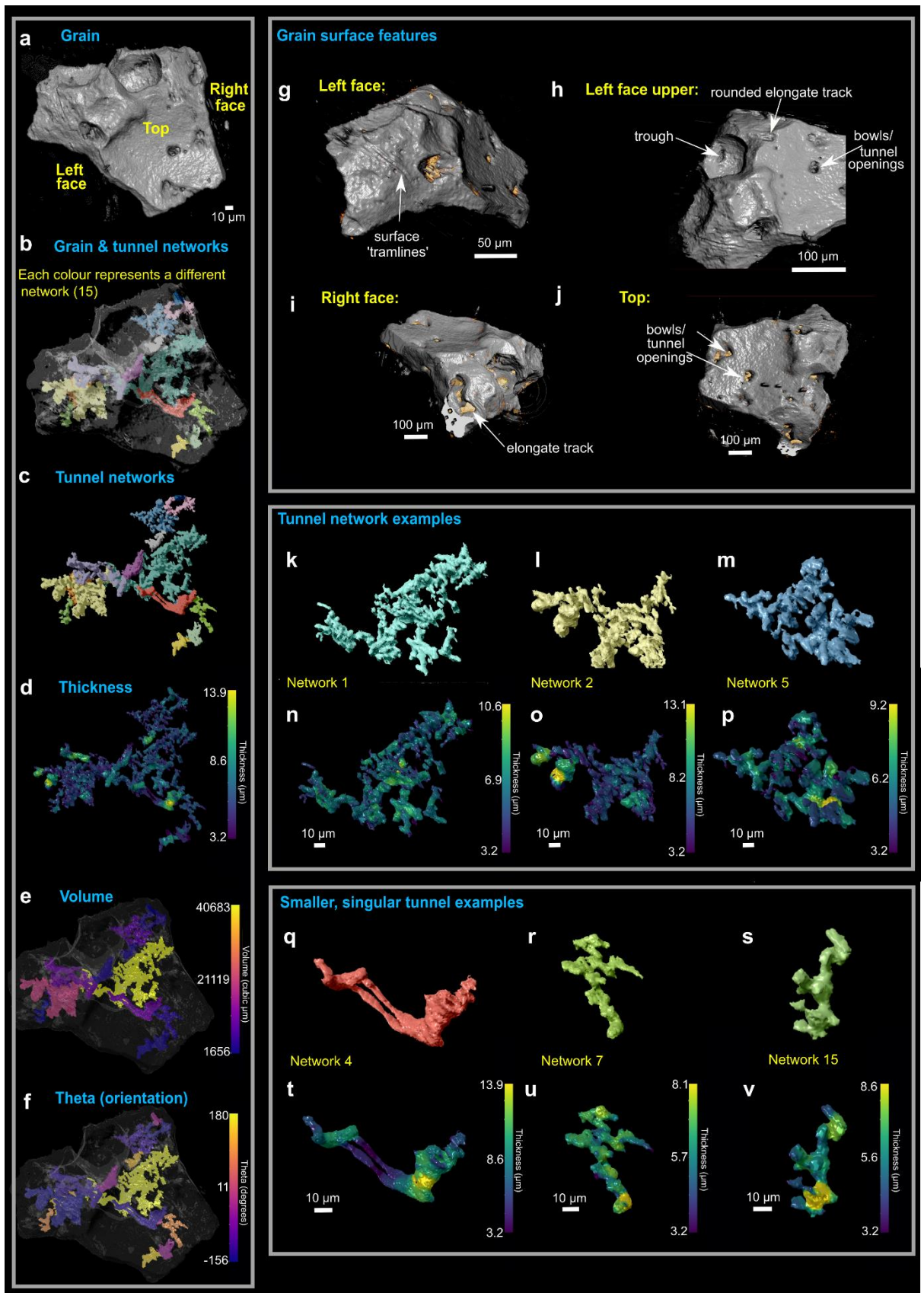
3D multi-scale imaging of soil core, subsurface segmentation, and grain (digital) isolation

      3D tomographic imaging of a CGC soil micro-core was achieved using the ZEISS Scout-and-Zoom workflow on a ZEISS Xradia 520 Versa XRM (Fig. 1). From initial whole-core scans (Fig. 1a, b), progressively higher magnification and resolution (i.e. smaller voxel sizes) in subsequent scans (Fig. 1c) enabled us to identify, target and image a ~300 µm diameter in-situ volcanic scoria grain from the central subsurface region of the micro-soil core (Supplementary Videos S1-2). The scans revealed that the grain has both surficial and internal features of interest visible to a voxel size of less than 1 µm (Fig. 1d, e, Supplementary Videos S3-4). Following segmentation of the grain and its internal features, these resolved into a) networks of branched and sometimes interconnected tunnels of varying morphologies

107 and characteristics (Figs 1e, 2a-f, k-v, Supplementary Video S3), and b) a series of holes and troughs

108 on the surface of the grain (Figs 1d, 2g-j).

109   The grain surface features are diverse, representing holes, troughs, and elongate tracks of

110 different orientations, lengths and shapes (Figs 2g-j). The tunnels appear to originate from holes at the

111 grain surface (Figs 1, 2a, g-j), which extend to varying depths within the grain, and also appear to

112 contain accumulations of organic material (Figs 2g-j), but these are at the limit of resolution of Versa

113 XRM. The individual tunnel networks were segmented for volumetric and morphological analyses, and

114 were provided with a specific colour for ease of locating them within the grain (Figs 2a-c). 3D

115 segmentation reveals that the tunnels make up 20% of the grain. The tunnel networks appear to fall into

116 two morphological groups: those that are branched (e.g. tunnel networks 1, 2 and 5; Figs 2 k-p) and

117 those that form singular, closed channels (e.g. tunnel networks 4, 7 and 15; Figs 2q-v). Performing

118 morphological analysis from the XRM segmentations reveals that all tunnels range in thickness from

119 3.2 to 13.9 µm (Fig. 2d) and the most voluminous are in the largest, most networked tunnels (e.g.

120 networks 1 and 2; Figs. 2e). The thickness varies throughout each of the networks, however the thickest

121 portion is usually at the entrance/exit hole (Figs 2k-v). Networks also don't have a particular orientation

122 in the grain and are varied across 360° (Fig 2f). Thus the tunnel networks can be characterised by their

123 shape, morphology, and the way that they branch.

124

Figure 2. 3D analysis of the segmented tunnel networks from the grain of interest. **(a-f)** The entire grain tunnel networks including each individual network segmented as its own colour **(a, b),** tunnel thickness

7

variations **(d)**, volume variations **(e)**, and orientation variations **(f)**. Grain surface features also shown **(g-j);** features include surface holes, tramlines, troughs, bowls, and rounded elongate tracks. Gold colour indicates accumulation of organic material. From analysis, there appears to be larger tunnel networks **(k-p)** and those that are more singular **(q-v)**; variations in thickness through the tunnels are shown. Also see Supplementary Videos in S3 for 3D visualisation of tunnel networks.
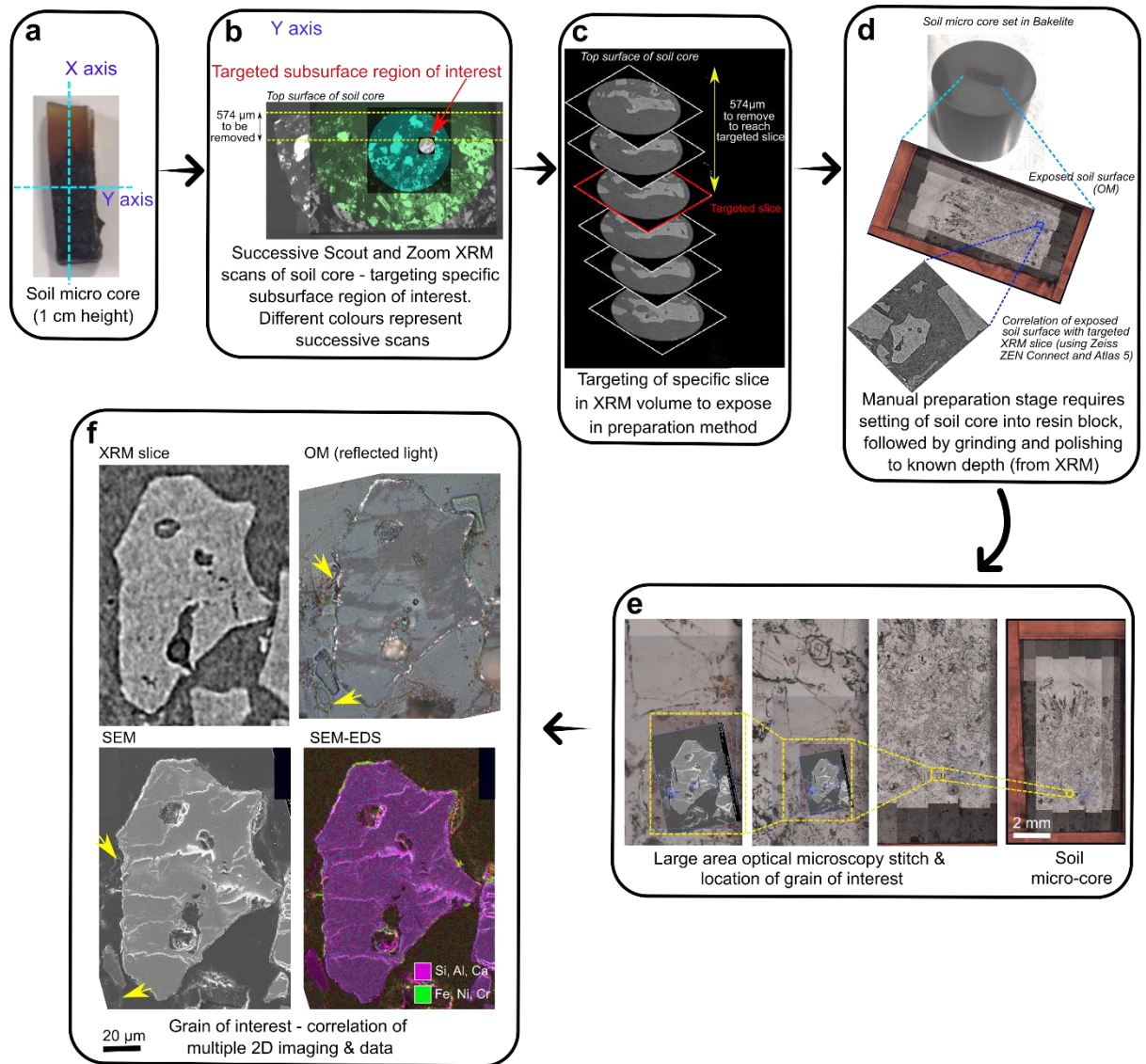
Figure 3. Additional correlative sample preparation step, revealing grain and slice of interest for further study via other imaging and chemical methods. **(a)** Axis orientations of soil micro-core. **(b)** Progressively higher resolution 3D volumes obtained from XRM are correlated, focussing on grain of interest (red arrow). **(c)** An assessment of depth of material to be removed (and from which axis) determined from XRM scans. Targeted slice from XRM scans at 574 µm depth. **(d)** Soil micro-core

138   mounted in bakelite, and manually ground and polished to remove specific depth of material (574 µm);

139   measurements taken regularly using a calliper (see methods section). **(e)** Large area stitch imaging was

140   completed via optical microscopy to image the grain of interest to high resolution in 2D. **(f)**

141   Subsequently the grain of interest underwent numerous 2D imaging and analysis methods including

142   SEM, OM, SEM-EDS, and correlation with the XRM slice. Yellow arrow indicates plant material

143   surrounding the grain within the soil matrix.

144

145   *Correlation of 2D and 3D datasets and correlative preparation step*

146   The correlative imaging workflow enables the combination of 3D and 2D datasets from multiple

147   modes of acquisition. By using advanced correlative software (ZEISS ZEN Connect and Atlas 5 (3D))

148   it is possible to target specific subsurface regions or features of interest from the 3D XRM data and

149   expose it through a separate correlative preparation step (Figs 3a-d), allowing further targeted study in

150   2D (i.e. through SEM imaging, SEM-EDS chemical mapping, FIB-SEM, or other techniques not used

151   here; Figs 3e-f). Subsequent imaging via OM and SEM of the same region is overlaid using ZEISS ZEN

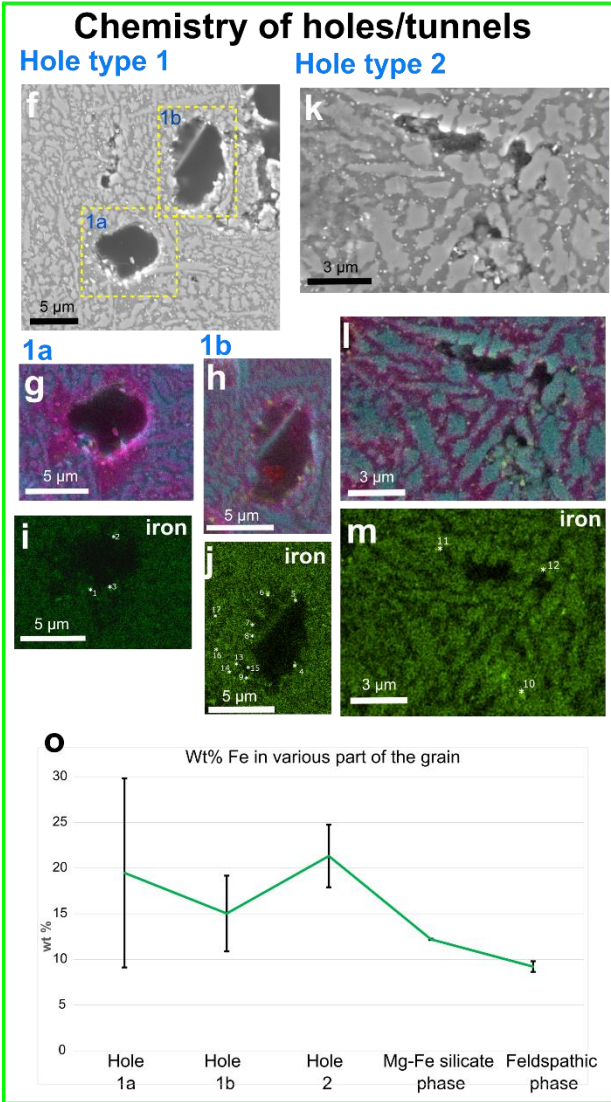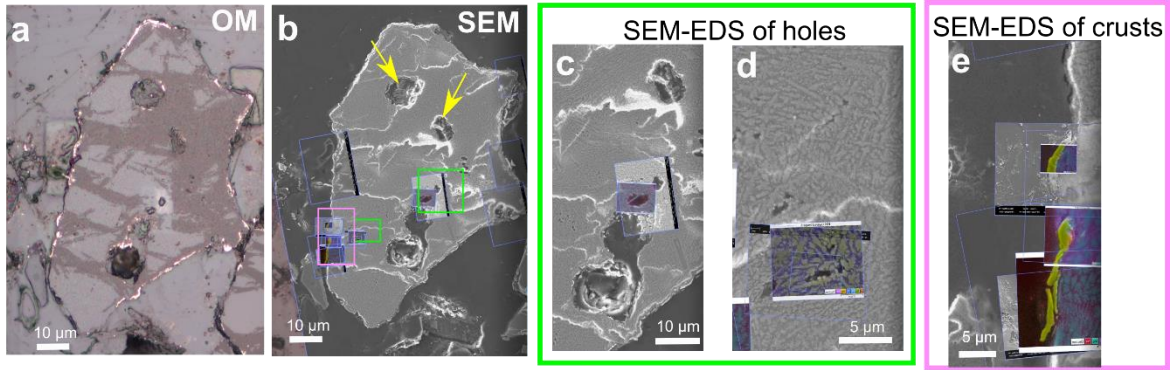152   Connect and combined with 3D XRM data (Fig. 3d, Supplementary Video S5).

153

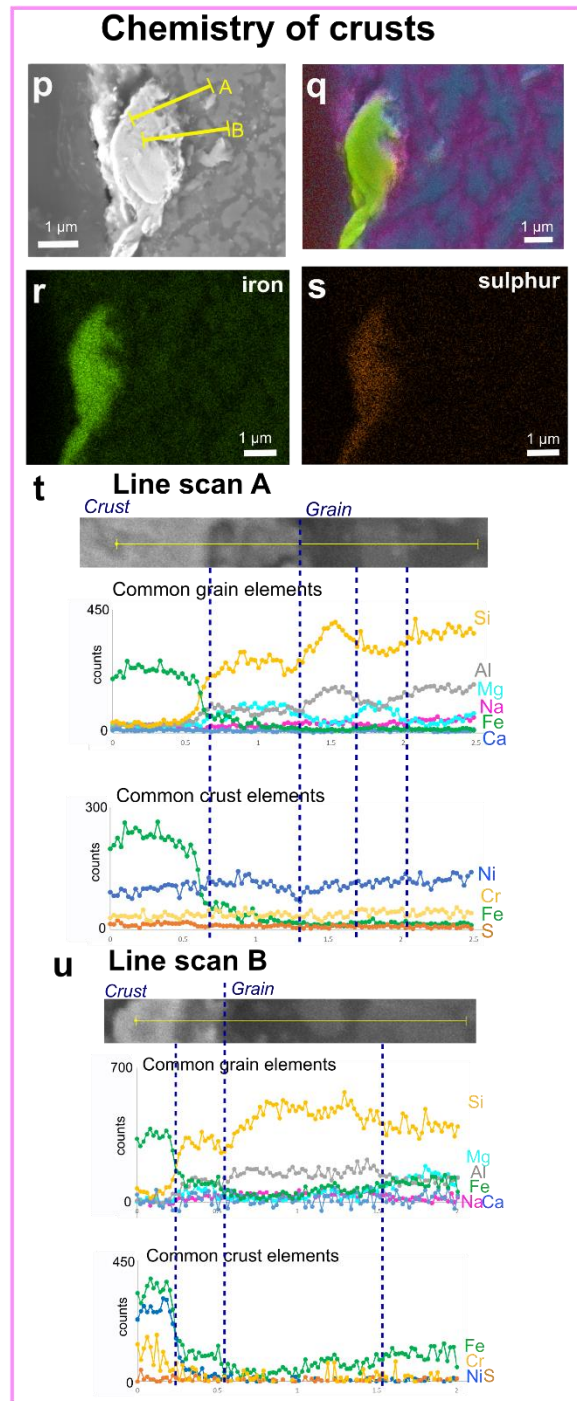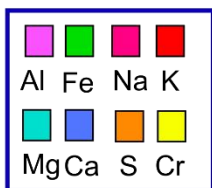154   *2D imaging of newly exposed grain surface (OM and SEM)*

155   SEM and OM imaging of the newly exposed volcanic glass grain surface reveals a

156   pseudosymplectite texture (Fig. 4); pseudo refers to the phases in this volcanic glass grain which are

157   not true minerals, and symplectite refers to a petrographic microstructure with intergrowths of two or

158   more phases where one (or more) phase may be more unstable than the other(s), and recrystalises during

159   formation to more stable constituents under changing pressures, temperatures, and/or interaction with

160   external fluids[46]. Chemical analysis of the grain via SEM-EDS indicates that there are two chemically

161   distinct psuedo-mineralogical phases in the symplectite: a brighter grey phase (from SEM greyscale

162   imaging) containing Mg, Ca, Fe and Si (interpreted as a Mg-Fe silicate phase), and a darker grey phase

163   (from SEM greyscale imaging) containing Al, Na, K, Si and O (interpreted as a feldspathic phase) (e.g.

164   Figs 4f-m, p-q). The grain contains large gas-escape vesicles (Fig. 4b) as well as the smaller tunnel

165   networks; the vesicles were omitted from the XRM segmentation process.

166   2D cross sections through tunnels of two different morphologies were investigated further, hereafter

167   named hole types 1 and 2 (Figs 4f-o). In hole type 1, sections reveal tunnels with a circular to elliptical

168   outline 5-10 µm in diameter (Figs 4f, g-j). Results show that these tunnels cut across the boundaries of

169   the feldspathic and Mg-Fe silicate phases. The tunnel outline is smooth and curved, where the rim is

170   bright in the SEM images, which appears to be due to the accumulation of heavier elements (Fe; Figs

171   4g-i).

a OM — 10 μm

b SEM — 10 μm

SEM-EDS of holes

c — 10 μm

d — 5 μm

SEM-EDS of crusts

e — 5 μm

Chemistry of holes/tunnels

Hole type 1

Hole type 2

f 1b, 1a — 5 μm

k — 3 μm

1a

g — 5 μm

1b

h — 5 μm

l — 3 μm

i iron — 5 μm

j iron — 5 μm

m iron — 3 μm

o Wt% Fe in various part of the grain

wt %

Hole 1a | Hole 1b | Hole 2 | Mg-Fe silicate phase | Feldspathic phase

chemical map and graph key

| Al | Fe | Na | K |
| Mg | Ca | S | Cr |

Chemistry of crusts

p A, B — 1 μm

q — 1 μm

r iron — 1 μm

s sulphur — 1 μm

t Line scan A

Crust — *Grain*

Common grain elements

counts — 450

Si, Al, Mg, Na, Fe, Ca

Common crust elements

counts — 300

Ni, Cr, Fe, S

u Line scan B

Crust — *Grain*

Common grain elements

counts — 700

Si, Mg, Al, Fe, Na, Ca

Common crust elements

counts — 450

Fe, Cr, Ni, S

172

173 **Figure 4. (a, b)** Correlation of 2D imaging (OM, SEM) views of exposed grain of interest. **(b)** location

174 of targeted areas of interest for SEM imaging and analysis via SEM-EDS. These were collected 'live'

175 to enable correlation to specific areas (Supplementary Video S5). Yellow arrows indicate vesicular gas

176 escape structures. Green box indicates holes of interest **(c, d),** while pink box represents grain surface

177 crusts **(e)**. **(f-m)** SEM imaging and SEM-EDS maps of tunnel cross sections (holes) from exposed

178 surface. Two types of hole are identified. Chemical and morphological variations in grain pseudo-

179 mineralogical phases also shown. **(o)** Weight % of Fe variations shown for different hole types and the

180 different pseudo-mineralogical phases; spot analyses locations shown in **(i-m)**. **(p-s)** SEM imaging and

181 chemical SEM-EDS maps of grain surface crusts shown; chemical line scans in **(p)** shown in **(t-u).** Y

182 axis in **(t-u)** is counts per second. The brighter grey mineralogical phase contains Mg, Ca, Fe and Si

183 (interpreted as a Mg-Fe silicate phase), and a darker grey mineralogical phase containing Al, Na, K, Si

184 and O (interpreted as a feldspathic phase). SEM images collected using SESI detector.

185

186   These accumulations appear nodulous and are often accompanied by high S but not always

187 (Supplementary Data S6). SEM-EDS spot analyses of the nodules indicate that Fe concentrations range

188 between 11 and 32 wt%, S is up to 1 wt%, and the average for hole type 1 is between 15 and 20 wt%.

189 The hole type 2 (Figs 4k-o) morphologies are irregularly shaped being more elongate and have a

190 diameter of ~1-2 µm. They formed entirely within the feldspathic (Al, Na, K, Si) phases leaving the

191 Mg-Fe silicate phase intact (Figs 4k-m). As with hole type 1, they contain Fe-rich nodular

192 accumulations on some hole edges (Figs 4l-m). SEM-EDS spot analysis indicates the nodules have Fe

193 concentrations ranging between 17 and 25 wt%, and negligible amounts of S (Supplementary Data S6).

194 The average chemical compositions of the Fe nodules in both hole types is higher than the Mg-Fe

195 silicate phase of the grain, with a larger variability particularly in hole 1a (Fig. 4o).

196   Reflected OM imaging indicates that there are bright regions on the outside edge of the grain

197 (Fig. 4a) forming irregular and non-continuous crusts. Further investigation via SEM indicates that the

198 crusts vary in morphology, generally forming 1-2 µm thick surface coatings that are not continuous

199 over the entire grain edge. Some crusts also appear as coatings within the larger gas escape vesicles

inside the grain (Fig. 4a). The boundary between the crust and the grain surface is sometimes abrupt, but often gradational, developing a mixed, transition layer (Fig. 4e, p). SEM-EDS analysis indicates that the crusts are an accumulation of heavier elements including Fe and S, where Fe is again in higher proportions compared with the 'background' Mg-Fe silicate phases of the grain (Fig. 4r). SEM-EDS line scans across the crust-grain boundary indicate abrupt chemical changes, particularly in Fe and Si, although low counts for Si are still collected in the crust. The transition layer appears to form an intermediate zone of mixed chemistry (Figs 4t, u).

*Nanotomography of tunnel and crust morphology from targeted FIB-SEM milling*
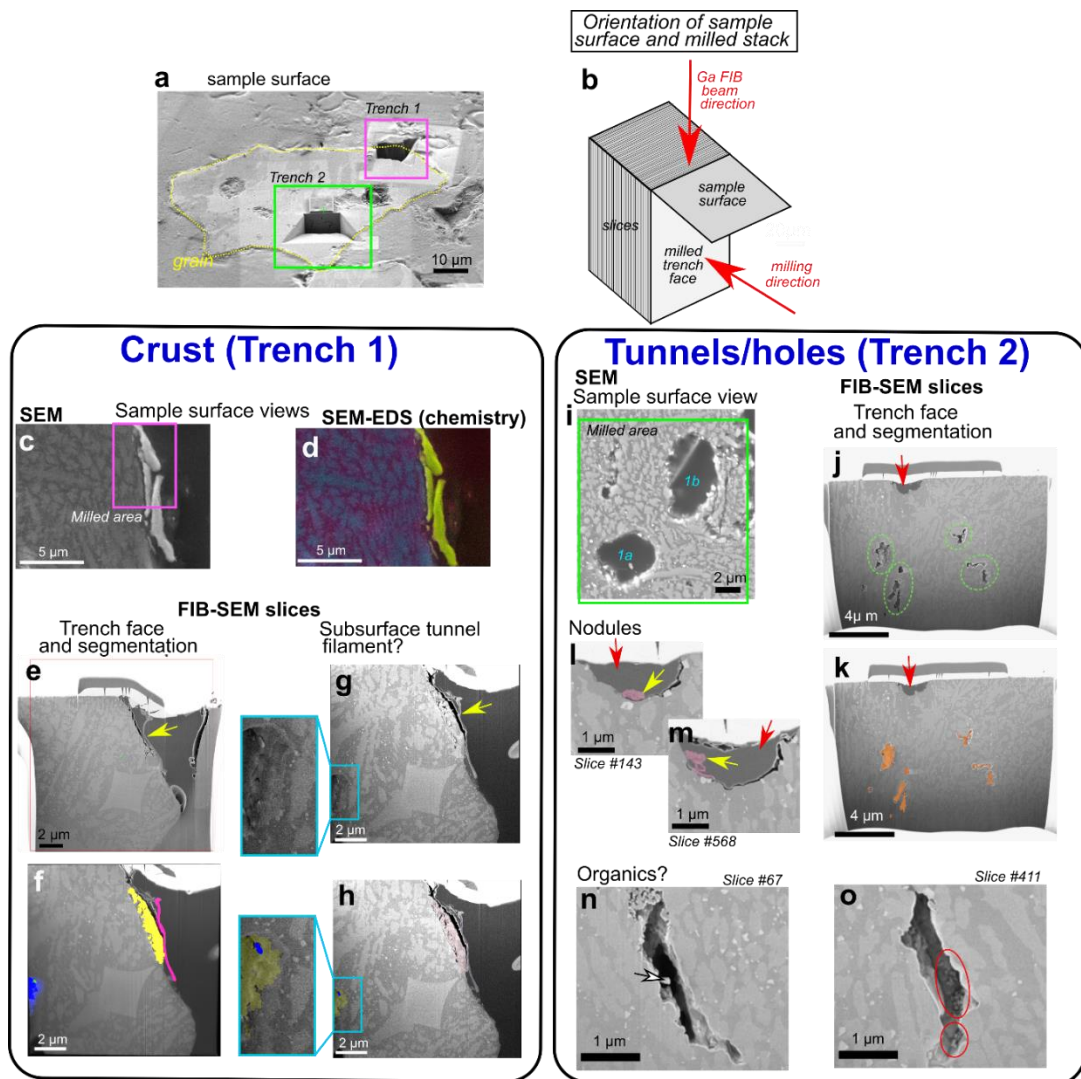
Figure 5. Location of FIB-SEM trenches and tomographic volumes. **(a)** Exposed grain from targeted XRM slice and surface material removal. Pink and green boxes highlight the location of milled trenches 1 and 2, respectively. **(b)** Schematic explaining the orientations associated with trench milling and sample surface. **(c-h)** Trench 1 (crust). Sample surface view **(c)**, accompanying chemical map (key the same as for Figure 4) **(d),** and view of the trench face after Atlas 5(3D) sample preparation and fine polish **(e-h);** yellow arrow indicates filamentous structure on crust. **(f, h)** Trench face highlighting false colour segmented components; yellow = crust, pink = filamentous portion of crust, blue = interior tunnel, green = (probable organic) filament within tunnel. **(g)** Final post-mill trench face highlighting subsurface tunnel containing a filament, with segmented version **(h). (i-o)** Trench 2 (tunnels/holes). **(i)** Sample surface view showing the milled area over hole types 1a,b from Figure 4. **(j, k)** Trench face highlighting subsurface tunnels that are unobservable from XRM imaging (green circles) and surface holes (red arrow). Segmented subsurface tunnels shown in **(k). (l, m)** Close up view of surface holes (red arrows) from two different slices through the volume highlighting segmented Fe nodules (yellow arrows). **(n, o)** Two examples of slices of subsurface tunnels, both exhibiting inhabiting potential organic filamentous (white arrow) and coccoid structures (red circle).

High resolution 3D volumes of the tunnels and the surface crusts were obtained through targeted FIB-SEM nanotomographic milling (Figs 5, 6). This not only complements the XRM imaging and data, but also enables further study of crust structure through combined higher resolution imaging and element analysis when XRM resolution limits are reached. Two trenches were destructively milled away using the Ga FIB beam, the locations and orientations of which are illustrated in Figs 5a, b; the scanning parameters of each can be found in Supplementary Methods S7. Milling and subsequent segmentation of a grain surface crust in trench 1 indicates an isolated subsurface crust of a different morphology to the rest of the grain, and a curious filamentous fragment appressed to the crust surface (Figs 5e-h). Additionally, a subsurface tunnel is observed which appears to contain a filamentous fragment (Figs 5g-h, box inset and enlargement). Because of the limited size of the milled volume, the extent of the subsurface tunnel through the rest of the grain is unclear.

237   Surface troughs and subsurface tunnels are also identified in milled trench 2 of tunnel/holes cross

238   sections (Figs 5i-o). The holes are infilled with embedding resin (Figs 5j-k, red arrows) and have smooth

239   and rounded sides (like their counterparts in Figs 4f-j). Subsurface tunnels are again identified; these

240   are more elongated, show greater irregularity, and appear to be located in both feldspathic and Mg-Fe

241   silicate phases (Figs 5j-o, 6d-e). Surface holes contain irregularly shaped nodular objects with some

242   filamentous structures (Figs 5l, m, yellow arrows). Finally, some subsurface tunnels seem to contain

243   filamentous and coccoid structures (Figs 5n, o, 6). 3D volumes of each FIB-SEM stack can be seen in

244   Fig. 6 and Supplementary Videos S8, 9.
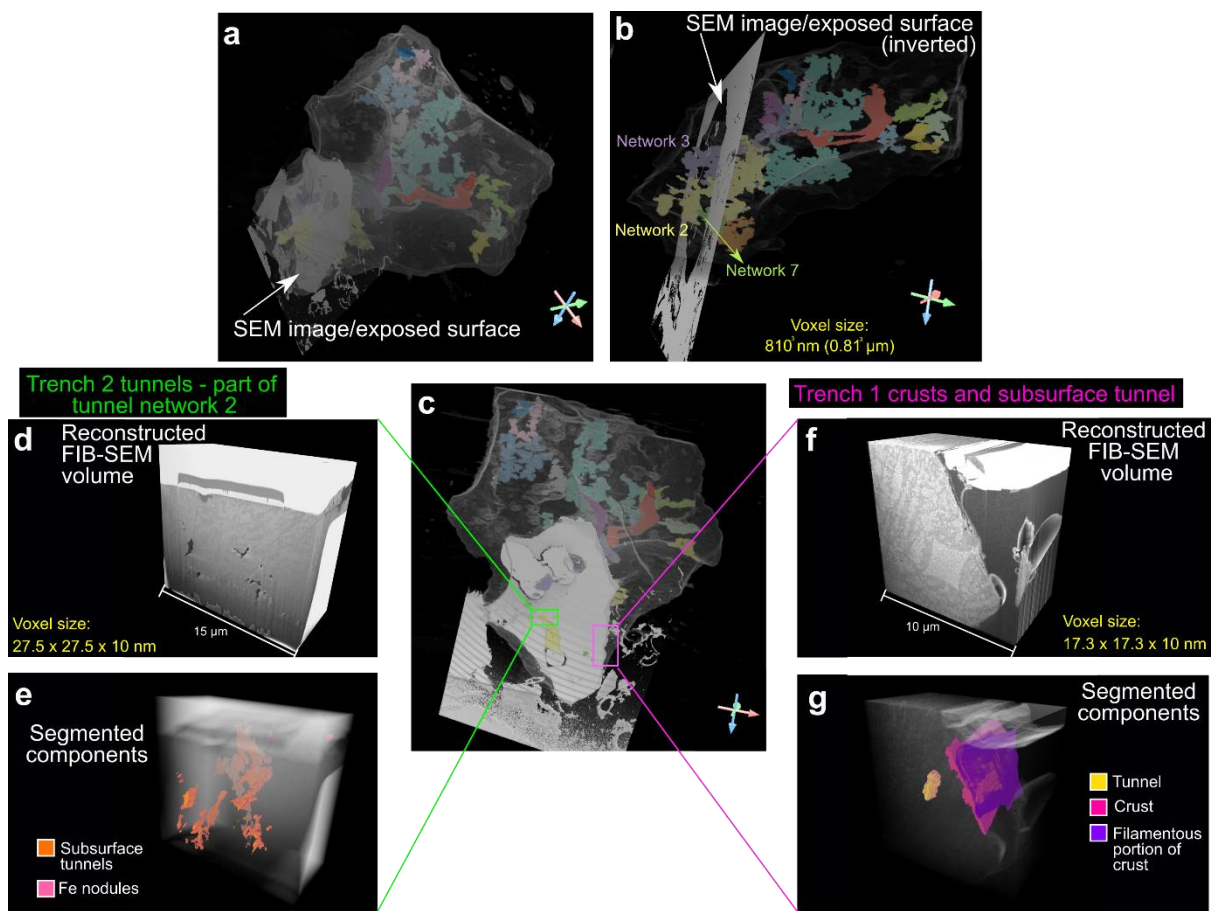
245

246   **Figure 6.** 3D XRM grain with segmented tunnels correlated with SEM image of exposed grain and

247   location of FIB-SEM volumes. **(a)** Location of SEM image/exposed surface in relation to the entire

248   grain, and which segmented tunnel networks interact with it (networks 2, 3 and 7) **(b)**. **(c)** Location of

249   FIB-SEM volumes for trench 2 (tunnels/holes) **(d, e)** and trench 1 (crusts) **(f, g).** Trench 2 tunnels are

250   identified as belonging to tunnel network 2 in Fig. 2.

15

251

Discussion

253   Our results demonstrate that multi-modal correlative microscopy provides a novel method for

254 understanding the multi-scale processes involved in soil weathering, specifically when these processes

255 (e.g. tunnel formation) occur in three dimensions. The correlative approach is becoming increasingly

256 used across the materials[36] and biological[38] sciences and has distinct advantages over conventional

257 'single mode' approaches. The correlative workflow overcomes the restriction of studying in one

258 scale/dimension/technique alone by combining (layering) imaging and other data (e.g., chemical,

259 crystallographic), while also successively improving resolution (Fig. 7, Supplementary Videos S1, 2,

260 5); for example, FIB-SEM pixel (voxel) sizes are vastly smaller than those obtained from conventional

261 laboratory XRM instruments (17.3 nm vs 0.81 µm for our results, respectively; Figs 6b and f,

262 Supplementary Methods S7, 10), allowing complementary analysis by bridging micro-to-nano scale

263 features with reciprocal context and improving information output (Fig. 6). Studying objects across

264 dimensions and scales also reveals characteristics and features which might not otherwise be identified

265 via a single technique or in one dimension alone (e.g. the morphology of tunnel networks and the

266 presence of grain crusts). Finally, the ability to target specific subsurface regions of the soil grain of

267 interest within a core sample through initial 'coarse' non-destructive 3D XRM imaging (Supplementary

268 Videos S1, 2), subsequent correlative preparation steps, and successive combined analytical and

269 imaging approaches enabled the study of a specific object in the context of its microenvironment (i.e.

270 the 'targeted trajectory approach' of [36]). Correlative imaging thus allows us to study the combined 2D

271 and 3D morphological and chemical characteristics of cryptogamic ground cover soil and grain

272 weathering.

273

274   Our findings demonstrate that an assortment of markings are present on the surface of a soil grain

275 of interest. These are reminiscent of the surficial bowls, tramlines, elongate troughs, and internal pore

276 networks previously described as biologically mediated weathering features (BWFs) by [21] that are

16

common in modern CGC soils. Although no microorganisms were observed colonising the grain surface

from our XRM scans (the voxel size is not small enough to resolve them; Supplementary Methods S10),

the presence of these features could suggest a biological origin. Indeed, accumulations of organic

material are present within holes and troughs (Figs 2g-i) and surrounding the grain in the soil matrix

(Fig. 3 f yellow arrows, Supplementary Videos S2, 4). This, to our knowledge, is the first description

of 3D surficial grain BWFs associated with CGCs.

3D volumetric analysis of tunnels, high resolution 2D imaging with chemical analysis, and the

correlation of datasets establishes that the holes/tunnel networks studied in Figs 4f-m, 5i-o belong to

tunnel network 2 (Figs 6a-c). The variations in morphology between the two types of tunnel (i.e. shape

and volume; Figs 2k-v) signify that they might have been formed by different processes; either abiotic

and/or biotic. One hypothesis could be the abiotic dissolution of easily weatherable mineral phases by

acid rain, which is a common atmospheric feature following recent eruptions in Iceland[47]. How much

this would affect proto-soil grains in CGCs though is unclear, and would be affected by the time the

grains were under chemical attack, depth of grains within the soil, and their proximity to eruptions. A

second hypothesis is that the tunnels formed through abiotic chemical dissolution where soil waters,

potentially enriched in CO_2, dissolved easily weatherable minerals. This could be exacerbated by below-

ground biological respiration of CO_2 and exudates from microbes could indirectly be responsible for

mineral attack and dissolution[48]. 2D imaging (Fig. 4) reveals evidence of hole formation that follows

specific localized grain chemistries (hole type 2; Figs 4k-m) where preferential dissolution occurs in

the feldspathic phase. This could indicate that these parts of the grain are more 'easily weatherable' and

prone to chemical attack. Interestingly, evidence of biologically mediated feldspar weathering is

common in the literature[29,30,49]; it is also reported that the presence of feldspars in rocks may increase

the susceptibility for biological attack by fungi, and that the rock's original chemistry and mineralogy

highly influences these physical and biochemical effects[50,51]. This is likely because feldspars contain

many of the essential elements (e.g. Ca, Na, K) needed for microorganisms and their symbiotic partners

to live[30,52]. Therefore, a third hypothesis is that the tunnel formation is due to biological factors. Hole

type 1 tunnel morphology cuts across chemical boundaries within the grain. This difference might be a

304   factor of time, where hole type 2 morphologies are created first and a longer duration of weathering

305   leads to the creation of larger, more rounded and branched tunnels (hole type 1). Hole type 1 has

306   rounded sides and circular cross section compared with type 2; these are reminiscent of 2D tunnel

307   structure observed in other studies[21,28] which are reported as being from a biological origin, usually

308   fungal[53]. Fungal tunnels within soil minerals have been explained as a result of dissolution and 'boring'

309   by combined biomechanical forcing and biochemical alteration; the tunnel retains its shape following

310   the death and degradation of the hyphae[27,49,50]. Other documented cases of fungal borings of mineral

311   grains produce tunnels of variable form, including simple/straight, branched, helical/coiled and

312   annulated[28,53], often with constant diameters and rounded ends[4,54], sometimes forming anastomosing

313   'channels'[29]. There is a single 3D study within garnets describing tunnels as straight and funnel-shaped

314   with rectangular cross sections becoming more rounded towards the tip[26]. In 2D, our results match

315   closely with these morphological descriptions from the literature, however in 3D our tunnels are not

316   uniform in shape or width (Fig. 2), being neither particularly straight nor funnel shaped, questioning

317   whether they can be attributed to fungi, or indeed, to a biological origin. Grain surficial holes/bowls,

318   which represent the openings of subsurface tunnels (Figs 1, 2), contain accumulations of organic

319   material (Figs 2g-j) implying intimate connections to living organisms. The tunnels might have formed

320   through chemical dissolution by bacterial communities rather than through biomechanical borings by

321   fungal hyphae. If this is the case, the feldspathic phase likely weathered first, and the Fe-Mg silicate

322   phase later, which creates the difference in tunnel morphologies. Fungal hyphae may have colonised

323   pre-existing cracks or fissures in the grain[50], the presence of which is supported by the identification of

324   surface BWFs likely caused by both fungal hyphae and bacteria[21]. So although we cannot be certain

325   what exactly was causing the tunnels, we have shown that by taking a correlative, multi-dimensional

326   and multi-scale approach, we have the ability to study weathering features in a more holistic way than

327   by one or two techniques alone.

328   FIB-SEM milling reveals potential communities of endolithic microbes evidenced by bacterial-like

329   filaments and coccoid-like structures within tunnels (Figs 5g-h, j-o), subsurface colonisation likely

330   providing protection from environmental extremes[50]. Although we cannot be sure what these organisms

331   are from FIB-SEM imaging alone, and the lack of evident internal structures, the shape and size suggest

they are not fungal hyphae, but could be a mix of cyanobacteria-fungi-lichen biofilms, lichenised and non-lichenised fungi, and yeast-like unicellular fungi, which commonly form endolithic microbial communities[5,50,55,56]. These organisms might have enhanced other forms of biologically mediated weathering through the in-situ secretion of organic acids and other exudates, leading to the irregular (non-straight/funnel) shape of the tunnels. Their existence is further supported by the presence of Fe-rich nodules in both types of tunnel (Figs 4g-m). Fe-rich nodules are thought to be indicators of fungal hyphae bio-precipitation in modern CGCs[21], with further occurrences reportedly created by lichens[57,58], bacteria[48], other fungi[59–61], and iron oxidising bacteria[62]. The Fe concentration of the nodules is higher than in the feldspathic and Mg-Fe silicate phases of the grain (Fig. 4o), indicating a separate source, which could be biologically derived. A biological source could also explain variations in Fe concentration observed in the nodules.

The imaging and analysis results presented here demonstrate that some surfaces of the grain of interest are covered in a crust of specific and distinctive chemical composition (high Fe and S; Figs 4, 5). XRM scans show some brightening of the surface indicating the presence of higher density material (Fig. 3f). However, because the crust thickness (<2 µm; Fig. 4) overlaps significantly with the voxel size resolution of the scans (0.81 µm), it cannot be conclusively segmented, which highlights the need to combine datasets from multiple modalities (and resolutions) through correlative microscopy. Our results demonstrate that crust morphology is variable, but because of their heavier element chemistry, they appear brighter in SEM and optical imaging, which is a phenomenon observed in other studies[63]. The crust chemical composition is distinctly different to the 'normal' composition of basaltic rocks and glass (Fig. 4), which indicates alternative modes of accumulation and formation. We discard the possibility that these crusts are due to contamination because a) there is evidence from the initial XRM scans, albeit at limited resolution, of bright areas on the outside of the grain; these precede any manual preparation, b) pristine grinding papers devoid of any contamination were used during the correlative preparation step, and c) the micro-soil core was already set in epoxy resin. One possible explanation could be the volcanic source of the grain. Nickel and chromium are common in early formed minerals

359 during volcanic eruption, where nickel can be incorporated into the forsterite (Mg end member of

360 olivine) chemical structure[64]. This however seems unlikely as the crusts are localised to grain surfaces

361 and don't appear to form internally. An alternative hypothesis could be that the patchy formation of the

362 crust on the grain surface could be due to localised biological interactions. Various rock varnishes,

363 coatings, weathering rinds and glazes are known[48,65,66], some specifically caused by fungi[50,66] and

364 epilithic lichens[50]. It is well established that key chemical diagnostic features of biologically-mediated

365 rock varnishes, glazes and coatings traditionally includes high accumulations of Mn and/or Fe[48,65,67,68].

366 Biomineralization of these elements as surface coatings, varnishes and glazes results from the

367 oxidation/reduction of the metal, usually because of excretion of oxalate and/or hydroxycarboxylic

368 acids by a variety of microbes including fungi and bacteria[48,50,58,69]. While the crusts outlined here do

369 not have significant accumulation of Mn, suggesting that Mn oxidising and reducing bacteria could be

370 absent from this CGC soil biosphere, they do have high Fe compared to the background grain chemistry

371 (Fig. 4). Lichenised fungi are known to biomineralize Fe-rich minerals on basaltic lava flows[69] and

372 lichenised cyanobacteria can biomineralize Fe hydroxides and clay-coatings to develop rock

373 varnishes[70,71]. Therefore, it could be that our crusts are produced by microbial bioprecipitation,

374 potentially by lichenised fungi and/or bacteria. Cr in the crusts could also be due to fungi, which can

375 precipitate reduced forms around their cells[69,72]. The presence and formation mechanism of these crusts

376 could be via the same processes as the Fe-rich nodules (Fig. 4); the composition of Fe is similar,

377 however the nodules appear to lack sufficient proportions of Cr and/or Ni. Although we cannot

378 conclusively state that the crusts are formed from biological interactions, it provides a plausible

379 hypothesis based on their morphology, chemical composition, the evidence for likely colonisation by

380 fungi and cyanobacteria from grain surface BWFs (Figs 2g-j), the subsurface weathering features, and

381 potential endolithic communities (Figs 1,2,4,5).
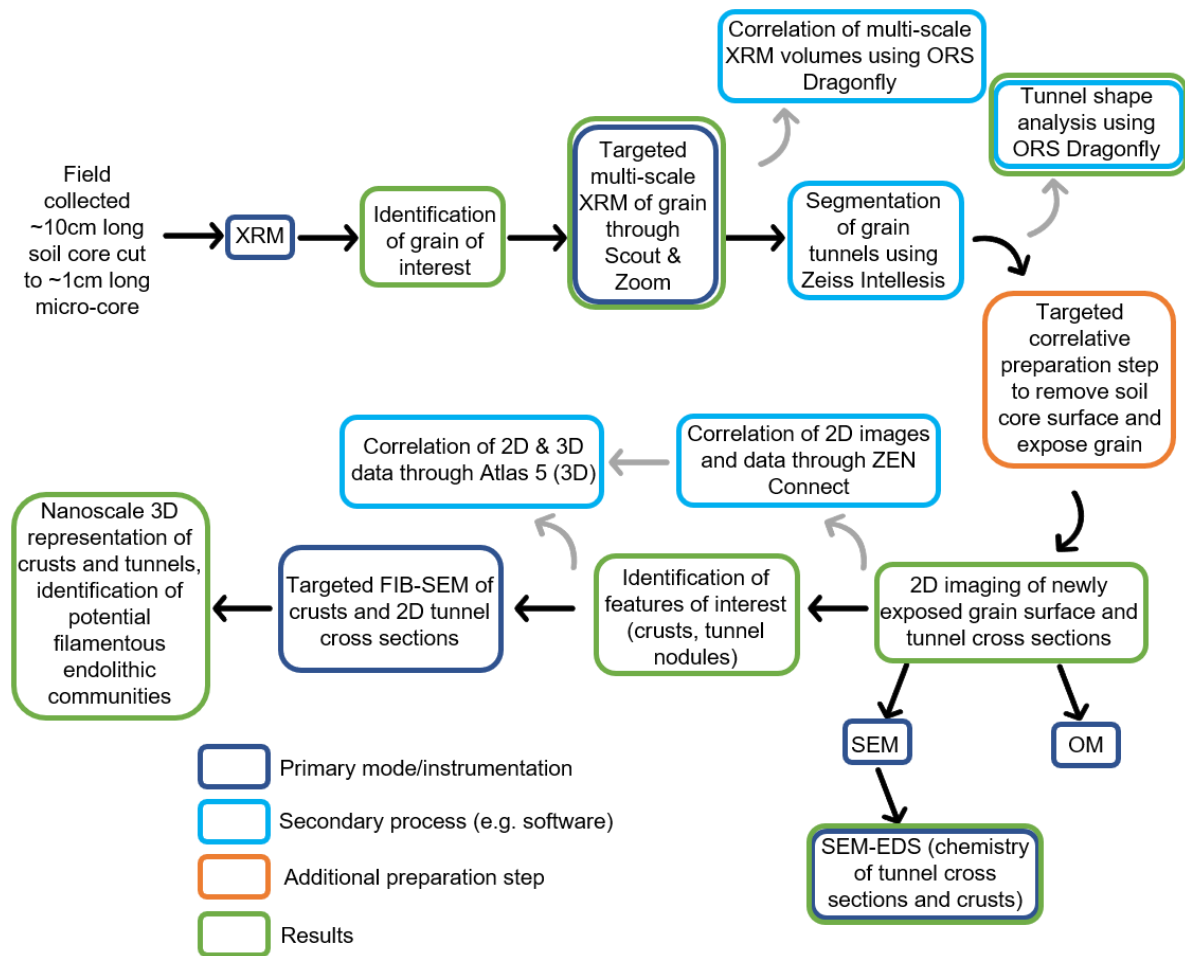
382

Figure 7. Flowchart summarising the targeted correlative workflow employed in this study.

383

384

Conclusions

385

386   This work highlights the advantages and novelty of using multi-scale and multi-dimensional

387   correlative microscopy to understand weathering in cryptogamic ground covers (CGCs), allowing

388   targeting of specific sub-surface soil regions for further study with complementary techniques. From

389   targeted multi-scale X-ray Microscopy (XRM) imaging, we have identified numerous surficial grain

390   features which are analogous to previously described biologically mediated weathering features

391   (BWFs) and internal tunnels, which are also likely the products of biological weathering processes,

392   whether directly from fungal borings or indirectly via mineral attack from microbial exudates. Two

393   types of tunnel were identified: those that form branched networks, and those that are more linear and

394   singular. Following exposure of a cross section of the grain of interest through an intermediate

395 correlative preparation step, we used optical microscopy (OM), scanning electron microscopy (SEM),

396 and element mapping (SEM-EDS) to characterise the morphology and chemical characteristics of the

397 tunnels. Results revealed micron-scale variations in morphology between the two types of tunnel and

398 Fe-rich nodules within, which were probably formed through biological processes. Grain surfaces crusts

399 were also identified. These have accumulations and variations in heavier elements (Fe, S), and could

400 represent a type of biological rock varnish/glaze. Further focused ion beam (FIB-SEM)

401 nanotomographic imaging of both tunnels and crusts not only improved resolution (voxel sizes) of

402 small-scale features, but also revealed the presence of probable biological filaments and coccoid-like

403 structures within tunnels. The presence of a) grain surface BWFs, b) Fe rich probable bioprecipitates,

404 and c) bacterial-like coccoid and filamentous forms within tunnels indicates that biology played an

405 important role in the alteration and weathering of the grain. The physical and chemical features outlined

406 here could be used as bioindicators to identify biologically mediated weathering in the rock record, and

407 potentially on extra-terrestrial bodies. There is a particular need for this to study the interactions

408 between Earth's earliest terrestrial biospheres and their substrates through the Proterozoic to the Earliest

409 Palaeozoic, particularly because of the disparity of the timing of terrestrialisation between molecular,

410 phylogenetic, and fossil information. Further studies should aim to quantify the biological interaction

411 with their substrates (in particular, soil grains) in real time and in multiple dimensions to better

412 understand biological weathering and the impact of micro-to-nano scale biogeochemical processes on

413 Earth-scale biogeochemical cycles.

414

415 **Methods**

416 - *Fieldwork and soil core collection*

417 CGCs were collected from various localities in Iceland, the core from this study sampled from 65

418 47.688'N, 16 46.384'W (location L1 in [4]). This core contained a mix of organisms including mosses

419 (*Racomitrum spp., Ceratodon purpureus, Pohlia sp., Polytrichum juniperinum)* and unidentified

420 lichens. An extensive description of the field site can be found in [21]. The core was cut and mounted in

421   epoxy resin for thin section preparation; following this the main soil core was cut down to ~1cm length

422   to enable ease of mounting (and improved resolution) in the XRM.

423

424   -   *X-ray Microscopy (XRM)*

425   Micro-soil cores were scanned using a ZEISS Xradia 520 Versa X-ray microscope (XRM) for 3D

426   tomography. The soil micro-core was attached using a cyanoacrylate-based adhesive to the end of a

427   ~2cm long pin and mounted onto a ZEISS specimen holder for scanning. Four scans were collected at

428   various magnifications and fields of view to utilise the Scout and Zoom feature of the scanner (see

429   Supplementary Methods S10); the final 'high resolution' scan being collected using the phase-enhanced

430   contrast method. The 'Scout and Zoom' feature enables multi-scale study within the same regions of

431   interest, enabling simple correlation of data at different scales (Supplementary Videos S1, 2).

432   Reconstructed .txm files were converted to 8bit greyscale 2D .tiff image stacks. Initially, tunnels were

433   identified in a grain of interest from a 2D .tiff stack (Supplementary Video S4), which was subsequently

434   segmented to reconstruct the pore structure in 3D (Supplementary Video S3). Segmentation of tunnels

435   was accomplished via the ZEISS ZEN Intellesis machine learning module within ZEISS ZEN Blue

436   software v. 2.6; a number of slices from the imaged volume (in this case, 6) were manually 'coloured

437   in' to reveal the different components within the scan (i.e. tunnels, grain, air) which was then applied

438   to the rest of the volume for segmentation. Visualisation and quantification of tunnel thickness, volume

439   and theta was achieved using Object Research Systems (ORS) Dragonfly software v. 2020.1. XRM

440   scans and Intellesis segmentation were undertaken within the Advanced Imaging of Materials (AIM)

441   Facility at Swansea University, UK, and ORS Dragonfly visualisation occurred within the Sheffield

442   Tomography Centre (STC) at the University of Sheffield, UK.

443

444   -   *Intermediate correlative microscopy sample preparation step*

445   Following the identification of a subsurface object of interest (in our case, the weathered grain)

446   preparations can be made to expose the object for further study via a preparation stage. In this step, a

23

447 'targeted slice' was chosen from the XRM data, and from that a known amount of sample surface

448 material (measured using the XRM scan images) can be removed. This is achieved via grinding and

449 polishing of the sample surface[73], and in our case, 574 µm (Fig. 3) needed to be removed to expose the

450 targeted region. For ease of material removal, the soil micro-core was mounted in conductive Bakelite

451 using an ATM Opal 410 mounting press, and subsequently ground and polished using sequentially finer

452 grinding papers (320-600-1200-4000 grit). The resin block was frequently measured using a Hilka

453 digital calliper to ensure the correct thickness of sample was removed. Further details on this manual

454 correlative sample preparation method can be found in [73]. Our results were within 20 µm of the targeted

455 slice (i.e., 544µm was removed), so a new XRM slice was chosen for the following image correlation

456 to match the newly exposed surface (Fig. 3); this 20 µm variation was likely due to the limited resolution

457 of the digital calliper (10 µm). The newly exposed grain surface, still set in the Bakelite resin block,

458 was coated with ~10 nm thickness of carbon using an Agar Scientific coater (Cressington, UK) for

459 subsequent SEM imaging and analysis. This process was undertaken within the Advanced Imaging of

460 Materials (AIM) Facility at Swansea University, UK.

461

462   -   *Correlative Microscopy – correlating datasets*

463   3D XRM data was initially loaded into ZEISS Atlas 5 (3D) software v. 5.2.1 installed on the ZEISS

464 Crossbeam 550 FIB-SEM within the Advanced Imaging of Materials (AIM) Facility at Swansea

465 University (UK). From there, once the specific amount of sample surface material had been removed

466 to expose the object of interest via the correlative preparation step, imaging and data derived from SEM,

467 SEM-EDS and OM were correlated manually using ZEISS ZEN Blue software v. 2.6 and the ZEISS

468 ZEN Connect module, enabling a variety of datatypes to be overlain (Supplementary Video S5). From

469 this, targeted FIB-SEM study was carried out utilising the combined 2D/3D approach in ZEISS Atlas 5

470 (3D) correlative software.

471

472   -   *Optical light microscopy (OM), Scanning Electron Microscopy (SEM) and energy dispersive*

473   *X-ray spectroscopy (EDS)*

474   Optical microscopy (OM) imaging was undertaken on a ZEISS Observer Z1M inverted microscope

475 using ZEISS ZEN Blue software v. 2.6 with ZEN Connect. SEM images and SEM-EDS chemical

476 analysis were undertaken on a ZEISS Crossbeam 550 FIB-SEM using Oxford Instruments X-MaxN 50

477 and Aztec software. A table illustrating the SEM imaging and data collection modes/analytical set up

478 can be found in Supplementary Methods S7. Imaging and analysis occurred within the Advanced

479 Imaging of Materials (AIM) Facility at Swansea University (UK).

480

481   -   *Focussed ion beam scanning electron microscopy (FIB-SEM)*

482   Nanotomographic volumes were collected for subsurface tunnels and surface crusts using a ZEISS

483 Crossbeam 550 gallium (Ga) source focussed ion beam scanning electron microscope (FIB-SEM) and

484 Atlas 5 (3D) correlative software v. 5.2.1. The sample preparation for nanotomographic milling is as

485 follows: After achieving an eucentric tilt correction, the sample stage is tilted to 54° so it is

486 perpendicular to the FIB column. The sample surface is lifted with the stage vertical axis to 5 mm where

487 the two columns are in alignment, and then fine-tuned to confirm the FIB and SEM beams are at a

488 coincidence point. Once an ROI is set using the overlay function of the Atlas 5 (3D) software (in our

489 cases 15 x 15 µm, and 10 x 7 µm; Figs 5c-o), setup can begin for the nanotomographic milling run.

490 Firstly, an initial platinum layer is deposited on the overlay area using a gas injection system and the

491 30kV 700 pA FIB probe. This protects the sample surface from damage by the Ga FIB beam and helps

492 to create a cleaner cross section. 3D tracking marks, which facilitate automatic alignment, focus,

493 astigmatism and drift correction as well as slice thickness tracking during the run, are milled onto the

494 platinum layer using the 30kV 50 pA FIB probe. These tracking marks are then infilled using the carbon

495 gas injection system to provide enough contrast between the platinum and the tracking marks. A trench

496 is then milled using the 30kV 7nA FIB probe to produce a cross sectional face to a depth of

497 approximately 15 µm. Finally, a lower energy probe is applied to the cross-sectional face using the

498 30kV 700 pA FIB probe for more precision and lower interaction volume. The cross-sectional face is

499 subsequently repeatedly milled (using the 30kV 700 pA FIB probe) and imaged (using the SEM SESI

500 detector with 1.8kV pA beam) to create individual images (or slices; 10nm thick) which can later be

501 reconstructed into a 3D volume. Voxel sizes for each run include 17.3 x 17.3 x 10 nm for trench 1, and

502 27.5 x 27.5 x 10 nm for trench 2. Further image collection parameters can be found in Supplementary

503 Methods S7. After a run of ~10 hours, the image stack is aligned using the Fiji/ImageJ plugin StackReg[74]

504 and cropped in three dimensions using the Fiji/ImageJ plugin Crop3D to remove unwanted redeposition

505 occasionally occurring on the edges of the imaged area. All 3D volumes (Figs 5, 6) were

506 visualised/rendered in ORS Dragonfly v. 2020.1. All of the above methods were conducted within the

507 Advanced Imaging of Materials (AIM) Facility at Swansea University, UK.

508

Data availability statement

510 Data is available in the supplemental materials.

References

512 1.   Morris, J. L. *et al.* The timescale of early land plant evolution. *Proc. Natl. Acad. Sci.*

513   201719588 (2018). doi:10.1073/pnas.1719588115

514 2.   Gibling, M. R. & Davies, N. S. Palaeozoic landscapes shaped by plant evolution. *Nat. Geosci.*

515   **5**, 99–105 (2012).

516 3.   Gibling, M. R. *et al.* Palaeozoic co-evolution of rivers and vegetation: A synthesis of current

517   knowledge. *Proc. Geol. Assoc.* **125**, 524–533 (2014).

518 4.   Mitchell, R. L. *et al.* Mineral weathering and soil development in the earliest land plant

519   ecosystems. *Geology* **44**, 1007–1010 (2016).

520 5.   Mergelov, N. *et al.* Alteration of rocks by endolithic organisms is one of the pathways for the

521   beginning of soils on Earth. *Sci. Rep.* **8**, 1–15 (2018).

522   6.   McMahon, W. J. & Davies, N. S. Evolution of alluvial mudrock forced by early land plants.

523   *Science (80-.).* **359**, 1022–1024 (2018).

524   7.   Field, K. J. *et al.* Functional analysis of liverworts in dual symbiosis with Glomeromycota and

525   Mucoromycotina fungi under a simulated Palaeozoic CO2 decline. *ISME J.* **10**, 1514–1526

526   (2016).

527   8.   Mills, B., Watson, A. J., Goldblatt, C., Boyle, R. & Lenton, T. M. Timing of Neoproterozoic

528   glaciations linked to transport-limited global weathering. *Nat. Geosci.* **4**, 861–864 (2011).

529   9.   Porada, P., Weber, B., Elbert, W., Pöschl, U. & Kleidon, A. Estimating impacts of lichens and

530   bryophytes on global biogeochemical cycles. *Global Biogeochem. Cycles* **28**, 71–85 (2014).

531   10.   Edwards, D., Cherns, L. & Raven, J. A. Could land-based early photosynthesizing ecosystems

532   have bioengineered the planet in mid-Palaeozoic times? *Palaeontology* **58**, 803–837 (2015).

533   11.   Williams, A. J., Buck, B. J. & Beyene, M. A. Biological Soil Crusts in the Mojave Desert,

534   USA: Micromorphology and Pedogenesis. *Soil Sci. Soc. Am. J.* **76**, 1685 (2012).

535   12.   Belnap, J. & Lange, O. L. *Biological Soil Crusts: Structure, Function, and Management*.

536   (Berlin Heidelberg, Springer-Verlag, 2001).

537   13.   Mitchell, R. L. *et al.* Cryptogamic ground covers as analogues for early terrestrial biospheres :

538   Initiation and evolution of biologically mediated soils. *Geobiology* **00**, 1–15 (2021).

539   14.   Kenrick, P., Wellman, C. H., Schneider, H. & Edgecombe, G. D. A timeline for

540   terrestrialization: Consequences for the carbon cycle in the Palaeozoic. *Philos. Trans. R. Soc.*

541   *B Biol. Sci.* **367**, 519–536 (2012).

542   15.   Strullu-Derrien, C., Wawrzyniak, Z., Goral, T. & Kenrick, P. Fungal colonization of the

543   rooting system of the early land plant Asteroxylon mackiei from the 407-Myr-old Rhynie

544   Chert (Scotland, UK). *Bot. J. Linn. Soc.* **179**, 201–213 (2015).

545   16.   Krings, M., Kerp, H., Hass, H., Taylor, T. N. & Dotzler, N. A filamentous cyanobacterium

546   showing structured colonial growth from the Early Devonian Rhynie chert. *Rev. Palaeobot.*

547   *Palynol.* **146**, 265–276 (2007).

548   17. Remy, W., Taylort, T. N., Hass, H. & Kerp, H. Four Hundred-million-year-old Vesicular

549   Arbuscular Mycorrhizae (Endomycorrhiae/ symbiosis/ fossil fungi /mutualims). *Proc. Natl.*

550   *Acad. Sci. United States Am.* **91**, 11841–11843 (1994).

551   18. Field, K. J. *et al.* Contrasting arbuscular mycorrhizal responses of vascular and non-vascular

552   plants to a simulated Palaeozoic CO2 decline. *Nat. Commun.* **3**, 1–8 (2012).

553   19. Lenton, T. M., Crouch, M., Johnson, M., Pires, N. & Dolan, L. First plants cooled the

554   Ordovician. *Nat. Geosci.* **5**, 86–89 (2012).

555   20. Mills, B. J. W., Batterman, S. A. & Field, K. J. Nutrient acquisition by symbiotic fungi

556   governs Palaeozoic climate transition. *Philos. Trans. R. Soc. B Biol. Sci.* **373**, (2018).

557   21. Mitchell, R. L., Strullu-Derrien, C. & Kenrick, P. Biologically mediated weathering in modern

558   cryptogamic ground covers and the early paleozoic fossil record. *J. Geol. Soc. London.* **176**,

559   430–439 (2019).

560   22. Furnes, H. *et al.* Comparing petrographic signatures of bioalteration in recent to Mesoarchean

561   pillow lavas: Tracing subsurface life in oceanic igneous rocks. *Precambrian Res.* **158**, 156–

562   176 (2007).

563   23. Smits, M. M. *et al.* Plant-driven fungal weathering: Early stages of mineral alteration at the

564   nanometer scale. *Geology* **37**, 615–618 (2009).

565   24. Bonneville, S. *et al.* Tree-mycorrhiza symbiosis accelerate mineral weathering: Evidences

566   from nanometer-scale elemental fluxes at the hypha-mineral interface. *Geochim. Cosmochim.*

567   *Acta* **75**, 6988–7005 (2011).

568   25. McLoughlin, N. Fungal origins? *Nat. Ecol. Evol.* **1**, 1–2 (2017).

569   26. Ivarsson, M. *et al.* Intricate tunnels in garnets from soils and river sediments in Thailand –

570   Possible endolithic microborings. *PLoS One* **13**, e0200351 (2018).

571   27.   Hoffland, E. *et al.* The Role of Fungi in Weathering. *Front. Ecol. Environ.* **2**, 258–264 (2004).

572   28.   McLoughlin, N., Furnes, H., Banerjee, N. R., Muehlenbachs, K. & Staudigel, H.

573   Ichnotaxonomy of microbial trace fossils in volcanic glass. *J. Geol. Soc. London.* **166**, 159–

574   169 (2009).

575   29.   Berner, R. A. & Cochran, M. F. Plant-induced weathering of Hawaiian basalts. *J. Sediment.*

576   *Res.* **68**, 723–726 (1998).

577   30.   Landeweert, R., Hoffland, E., Finlay, R. D., Kuyper, T. W. & Van Breemen, N. Linking plants

578   to rocks: Ectomycorrhizal fungi mobilize nutrients from minerals. *Trends Ecol. Evol.* **16**, 248–

579   254 (2001).

580   31.   Van Schöll, L. *et al.* Rock-eating mycorrhizas: Their role in plant nutrition and

581   biogeochemical cycles. *Plant Soil* **303**, 35–47 (2008).

582   32.   Quirk, J. *et al.* Evolution of trees and mycorrhizal fungi intensifies silicate mineral weathering.

583   *Biol. Lett.* **8**, 1006–1011 (2012).

584   33.   Daly, M. *et al.* A multi-scale correlative investigation of ductile fracture. *Acta Mater.* **130**, 56–

585   68 (2017).

586   34.   Gelb, J., Finegan, D. P., Brett, D. J. L. & Shearing, P. R. Multi-scale 3D investigations of a

587   commercial 18650 Li-ion battery with correlative electron- and X-ray microscopy. *J. Power*

588   *Sources* **357**, 77–86 (2017).

589   35.   Slater, T. J. A. *et al.* Multiscale correlative tomography: An investigation of creep cavitation in

590   316 stainless steel. *Sci. Rep.* **7**, 1–10 (2017).

591   36.   Burnett, T. L. & Withers, P. J. Completing the picture through correlative characterization.

592   *Nat. Mater.* **18**, 1041–1049 (2019).

593   37.   Mitchell, R. L. *et al.* Macro-to-nanoscale investigation of wall-plate joints in the acorn

594   barnacle Semibalanus balanoides : correlative imaging , biological form and function , and

595   bioinspiration. *J. R. Soc. Interface* **16**, 20190218 (2019).

596 38. Bradley, R. S. & Withers, P. J. Correlative multiscale tomography of biological materials.

597   *MRS Bull.* **41**, 549–556 (2016).

598 39. Ferstl, S. *et al.* Nanoscopic X-ray tomography for correlative microscopy of a small

599   meiofaunal sea-cucumber. *Sci. Rep.* **10**, 1–12 (2020).

600 40. O'Sullivan, J. D. B., Cruickshank, S. M., Starborg, T., Withers, P. J. & Else, K. J.

601   Characterisation of cuticular inflation development and ultrastructure in Trichuris muris using

602   correlative X-ray computed tomography and electron microscopy. *Sci. Rep.* **10**, 1–9 (2020).

603 41. Goral, J., Walton, I., Andrew, M. & Deo, M. Pore system characterization of organic-rich

604   shales using nanoscale- resolution 3D imaging. *Fuel* **258**, 116049 (2019).

605 42. Andrew, M. Comparing organic-hosted and intergranular pore networks: topography and

606   topology in grains, gaps and bubbles. *Geol. Soc. London, Spec. Publ.* **484**, SP484.4 (2018).

607 43. Ma, L. *et al.* Correlative multi-scale imaging of shales: a review and future perspectives. *Geol.*

608   *Soc. London, Spec. Publ.* **454**, 175–199 (2017).

609 44. Schlüter, S., Eickhorst, T. & Mueller, C. W. Correlative Imaging Reveals Holistic View of

610   Soil Microenvironments. *Environ. Sci. Technol.* **53**, 829–837 (2019).

611 45. Bandara, C. D. *et al.* High-Resolution Chemical Mapping and Microbial Identification of

612   Rhizosphere using Correlative Microscopy. *bioRxiv* 1–26 (2021).

613 46. Spruzeniece, L., Piazolo, S., Daczko, N. R., Kilburn, M. R. & Putnis, A. Symplectite

614   formation in the presence of a reactive fluid: insights from hydrothermal experiments. *J.*

615   *Metamorph. Geol.* **35**, 281–299 (2017).

616 47. Stefánsson, A. *et al.* Major impact of volcanic gases on the chemical composition of

617   precipitation in Iceland during the 2014–2015 Holuhraun eruption. *Jounral Geophys. Res.*

618 *Atmos. Geophys. Res. Atmos.* **122**, 1971–1982 (2017).

619 48. Gadd, G. M. Metals, minerals and microbes: Geomicrobiology and bioremediation.

620 *Microbiology* **156**, 609–643 (2010).

621 49. Jongmans, A. G. *et al.* Rock-eating fungi. **389**, 682–683 (1997).

622 50. Gadd, G. M. Fungi, Rocks, and Minerals. *Elements* **13**, 171–176 (2017).

623 51. Warscheid, T. & Braams, J. Biodeterioration of stone: a review. *Int. Biodeterior.*

624 *Biodegredation* **46**, 343–368 (2000).

625 52. Burghelea, C. *et al.* Mineral nutrient mobilization by plants from rock: influence of rock type

626 and arbuscular mycorrhiza. *Biogeochemistry* **124**, 187–203 (2015).

627 53. Mcloughlin, N., Staudigel, H., Furnes, H., Eickmann, B. & Ivarsson, M. Mechanisms of

628 microtunneling in rock substrates: Distinguishing endolithic biosignatures from abiotic

629 microtunnels. *Geobiology* **8**, 245–255 (2010).

630 54. Hoffland, E., Giesler, R., Jongmans, T. & Van Breemen, N. Increasing feldspar tunneling by

631 fungi across a North Sweden podzol chronosequence. *Ecosystems* **5**, 11–22 (2002).

632 55. Wierzchos, J., de los Ríos, A. & Ascaso, C. Microorganisms in desert rocks: The edge of life

633 on Earth. *Int. Microbiol.* **15**, 173–183 (2012).

634 56. Ascaso, C. & Wierzchos, J. New approaches to the study of Antarctic lithobiontic

635 microorganisms and their inorganic traces, and their application in the detection of life in

636 Martian rocks. *Int. Microbiol.* **5**, 215–222 (2003).

637 57. Gorbushina, A. A., Boettcher, M., Brumsack, H. J., Krumbein, W. E. & Vendrell-Saz, M.

638 Biogenic forsterite and opal as a product of biodeterioration and lichen stromatolite formation

639 in table mountain systems (Tepuis) of Venezuela. *Geomicrobiol. J.* **18**, 117–132 (2001).

640 58. Adamo, P. & Violante, P. Weathering of rocks and neogenesis of minerals associated with

641 lichen activity. *Appl. Clay Sci.* **16**, 229–256 (2000).

642   59.   Oggerin, M., Tornos, F., Rodriguez, N., Pascual, L. & Amils, R. Fungal Iron

643   Biomineralization in Río Tinto. *Minerals* **6**, 37 (2016).

644   60.   Akhtar, M. E. & Kelso, W. I. Electron microscopic characterisation of iron and manganese

645   oxide/hydroxide precipitates from agricultural field drains. 1. *Biol. Fertil. Soils* **16**, 305–312

646   (1993).

647   61.   Gadd, G. M. Fungal production of citric and oxalic acid: importance in metal speciation,

648   physiology and biogeochemical processes. *Advances in microbial physiology* **41**, 47–92

649   (1999).

650   62.   Napieralski, S. A. *et al.* Microbial chemolithotrophy mediates oxidative weathering of granitic

651   bedrock. *Proc. Natl. Acad. Sci. U. S. A.* **116**, 26394–26401 (2019).

652   63.   Dorn, R. I., Mahaney, W. C. & Krinsley, D. H. Case Hardening: Turning Weathering Rinds

653   into Protective Shells. *Elements* **13**, 165–169 (2017).

654   64.   Schreiber, H. D. Experimental studies of nickel and chromium partitioning into olivine from

655   synthetic basaltic melts. in *Lunar and Planetary Science Conference, 10th, Houston, Texas,*

656   *Proceedings Volume 1* 509–516 (1979).

657   65.   Burford, E. P., Kierans, M. & Gadd, G. M. Geomycology: Fungi in mineral substrata.

658   *Mycologist* **17**, 98–107 (2003).

659   66.   Dorn, R. I., Gordon, S. J., Krinsley, D. & Langworthy, K. Nanoscale: Mineral Weathering

660   Boundary. in *Treatise on Geomorphology* (eds. Shroder, J. & Pope, G. A.) **4**, 44–69 (2013).

661   67.   Smits, M. Mineral tunneling by fungi. in *Fungi in Biogeochemical cycles* (ed. Gadd, G. M.)

662   311–327 (Cambridge University Press, 2006).

663   68.   Gorbushina, A. A. Life on the rocks. *Environ. Microbiol.* **9**, 1613–1631 (2007).

664   69.   Gadd, G. M. Geomycology: biogeochemical transformations of rocks, minerals, metals and

665   radionuclides by fungi, bioweathering and bioremediation. *Mycol. Res.* **111**, 3–49 (2007).

666   70.   Arocena, J. M., Zhu, L. P. & Hall, K. Mineral accumulations induced by biological activity on

667   granitic rocks in Qinghai Plateau, China. *Earth Surf. Process. Landforms* **28**, 1429–1437

668   (2003).

669   71.   Krumbein, W. E. & Jens, K. Biogenic rock varnishes of the Negev desert (Israel) an ecological

670   study of iron and manganese transformation by cyanobacteria and fungi. *Oecologia* **50**, 25–38

671   (1981).

672   72.   Gadd, G. M. Microbial formation and transformation of organometallic and organometalloid

673   compounds. *FEMS Microbiol. Rev.* **11**, 297–316 (1993).

674   73.   Mitchell, R. L. *et al.* What Lies Beneath : 3D vs 2D Correlative Imaging Challenges and How

675   to Overcome Them. *Microsc. Microanal.* **25**, 416–417 (2019).

676   74.   Thévenaz, P., Ruttimann, U. E. & Unser, M. A pyramid approach to subpixel registration

677   based on intensity. *IEEE Trans. Image Process.* **7**, 27–41 (1998).

678

679

689

690

Figure legends

Figure 1. The correlative 3D imaging process: illustrates progressive higher resolution study from whole CGC soil core **(a),** to micro-core, Scout and Zoom feature on ZEISS Xradia Versa 520 **(b, c),** and finally segmentation of grain tunnels **(d, e)** (also see Supplementary Videos S1-3).

Figure 2. 3D analysis of the segmented tunnel networks from the grain of interest. **(a-f)** The entire grain tunnel networks including each individual network segmented as its own colour **(a, b),** tunnel thickness variations **(d)**, volume variations **(e)**, and orientation variations **(f)**. Grain surface features also shown

34

714   **(g-j);** features include surface holes, tramlines, troughs, bowls, and rounded elongate tracks. Gold

715   colour indicates accumulation of organic material. From analysis, there appears to be larger tunnel

716   networks **(k-p)** and those that are more singular **(q-v);** variations in thickness through the tunnels are

717   shown. Also see Supplementary Video S3.

718

719   **Figure 3.** Additional correlative sample preparation step, revealing grain and slice of interest for further

720   study via other imaging and chemical methods. **(a)** Axis orientations of soil micro-core. **(b)**

721   Progressively higher resolution 3D volumes obtained from XRM are correlated, focussing on grain of

722   interest (red arrow). **(c)** An assessment of depth of material to be removed (and from which axis)

723   determined from XRM scans. Targeted slice from XRM scans at 574 µm depth. **(d)** Soil micro-core

724   mounted in bakelite, and manually ground and polished to remove specific depth of material (574 µm);

725   measurements taken regularly using a calliper (see methods section). **(e)** Large area stitch imaging was

726   completed via optical microscopy to image the grain of interest to high resolution in 2D. **(f)**

727   Subsequently the grain of interest underwent numerous 2D imaging and analysis methods including

728   SEM, OM, SEM-EDS, and correlation with the XRM slice. Yellow arrow indicates plant material

729   surrounding the grain within the soil matrix.

730

731   **Figure 4. (a, b)** Correlation of 2D imaging (OM, SEM) views of exposed grain of interest. **(b)** location

732   of targeted areas of interest for SEM imaging and analysis via SEM-EDS. These were collected 'live'

733   to enable correlation to specific areas (Supplementary Video S5). Yellow arrows indicate vesicular gas

734   escape structures. Green box indicates holes of interest **(c, d),** while pink box represents grain surface

735   crusts **(e)**. **(f-m)** SEM imaging and SEM-EDS maps of tunnel cross sections (holes) from exposed

736   surface. Two types of hole are identified. Chemical and morphological variations in grain mineralogical

737   phases also shown. **(o)** Wt% of Fe variations shown for different hole types and the different

738   mineralogical phases; spot analyses locations shown in **(i-m)**. **(p-s)** SEM imaging and chemical SEM-

739   EDS maps of grain surface crusts shown; chemical line scans in **(p)** shown in **(t-u).** Y axis in **(t-u)** is

counts per second. The brighter grey mineralogical phase contains Mg, Ca and Fe (interpreted as a Mg-Fe silicate phase), and a darker grey mineralogical phase containing Al, Na, K, Si and O (interpreted as a feldspathic phase). SEM images collected using SESI detector.

Figure 5. Location of FIB-SEM trenches and tomographic volumes. **(a)** Exposed grain from targeted XRM slice and surface material removal. Blue boxes highlight the milled trenches (1 and 2) **(b)** Schematic explaining the orientations associated with trench milling and sample surface. **(c-h)** Trench 1 (crust). Sample surface view **(c)**, accompanying chemical map (key the same as for Figure 4) **(d)**, and view of the trench face after Atlas 5(3D) sample preparation and fine polish **(e-h);** yellow arrow indicates filamentous structure on crust. **(f, h)** Trench face highlighting false colour segmented components; yellow = crust, pink = filamentous portion of crust, blue = interior tunnel, green = (probable organic) filament within tunnel. **(g)** Final post-mill trench face highlighting subsurface tunnel containing a filament, with segmented version **(h). (i-o)** Trench 2 (tunnels/holes). **(i)** Sample surface view showing the milled area over hole types 1a,b from Figure 4. **(j, k)** Trench face highlighting subsurface tunnels that are unobservable from XRM imaging (green circles) and surface holes (red arrow). Segmented subsurface tunnels shown in **(k). (l, m)** Close up view of surface holes (red arrows) from two different slices through the volume highlighting segmented Fe nodules (yellow arrows). **(n, o)** Two examples of slices of subsurface tunnels, both exhibiting inhabiting potential organic filamentous (white arrow) and coccoid structures (red circle).

Figure 6. 3D XRM grain with segmented tunnels correlated with SEM image of exposed grain and location of FIB-SEM volumes. **(a)** Location of SEM image/exposed surface in relation to the entire grain, and which segmented tunnel networks interact with it (networks 2, 3 and 7) **(b). (c)** Location of FIB-SEM volumes for trench 2 (tunnels/holes) **(d, e)** and trench 1 (crusts) **(f, g).** Trench 2 tunnels are identified as belonging to tunnel network 2 in Fig. 2.

Figure 7. Flowchart summarising the targeted correlative workflow employed in this study.

766